Chemical Engineering Journal 368 (2019) 438–447

Contents lists available at ScienceDirect

Chemical Engineering Journal

journal homepage: www.elsevier.com/locate/cej

Hierarchical yolk-shell CNT-(NiCo)O/C microspheres prepared by one-pot spray pyrolysis as anodes in lithium-ion batteries

Se Hwan Oh[a], Min Su Jo[a], Sang Mun Jeong[b], Yun Chan Kang[c,*], Jung Sang Cho[a,*]

[a] Department of Engineering Chemistry, Chungbuk National University, Chungbuk 361-763, Republic of Korea
[b] Department of Chemical Engineering, Chungbuk National University, Chungbuk 361-763, Republic of Korea
[c] Department of Materials Science and Engineering, Korea University, Anam-Dong, Seongbuk-Gu, Seoul 136-713, Republic of Korea

HIGHLIGHTS

- Hierarchical yolk–shell-microsphere was prepared by one-pot process in 6 s.
- CNT-(NiCo)O/C yolk frame was composed and linked with CNTs.
- Detailed formation mechanism of the microsphere was investigated.
- Unique architecture showed excellent Li ion storage properties.

GRAPHICAL ABSTRACT

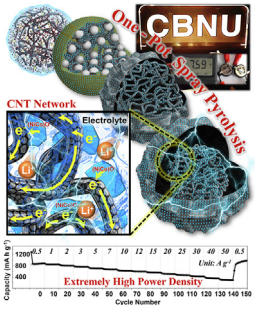

ARTICLE INFO

Keywords:
Yolk-shell
Spray pyrolysis
Lithium ion batteries
Anode materials
(Ni,Co)O solid solution

ABSTRACT

This paper presents a hierarchical yolk–shell-structured microsphere comprising a hierarchical carbon nanotube (CNT)-(NiCo)O/C yolk and an embossed hollow thin shell (hereafter denoted as CNT-(NiCo)O/C microsphere) prepared by a one-pot spray pyrolysis process for potential use as an anode in lithium-ion batteries. During spray pyrolysis, the hierarchical CNT-(NiCo)O/C yolk, whose frame is linked with CNTs, is formed by mutual binding of the CNTs and size-controlled polystyrene (PS) nanobeads and subsequent selective decomposition of these nanobeads. Further, phase separation of melted poly(vinylpyrrolidone) facilitates the formation of the hollow shell. The discharge capacity of the CNT-(NiCo)O/C microspheres after 1000 cycles at an extremely high current density of 5.0 A g^{-1} is 598 mA h g^{-1}. The CNT-(NiCo)O/C microspheres show reversible discharge capacities of 886, 709, 509, and 294 mA h g^{-1} at current densities of 0.5, 5, 20, and 50 A g^{-1}, respectively. The unique nanostructure of the CNT-(NiCo)O/C microspheres with high electrical conductivity promotes the transfer kinetics of electrons and Li^+ ions, which consequently leads to their improved electrochemical performances.

1. Introduction

In recent years, anode materials for lithium-ion batteries (LIBs) have been required to have high energy and power densities and long cycle stability in view of the use of LIBs in power systems [1–6]. Transition metal oxides (TMOs), which store Li-ions via a conversion reaction, have been considered to be efficient anode materials because of their low cost, eco-friendliness, and high theoretical capacity [7–13]. However, due to the intrinsic characteristics of TMOs, such as large volume expansion during the lithiation–delithiation process and low electrical conductivity, they exhibit poor cyclic and rate performances [14–19]. The choice of compounds of TMOs and their nanostructure design have

* Corresponding authors.
E-mail addresses: yckang@korea.ac.kr (Y.C. Kang), jscho@cbnu.ac.kr (J.S. Cho).

https://doi.org/10.1016/j.cej.2019.02.144
Received 20 November 2018; Received in revised form 18 January 2019; Accepted 19 February 2019
Available online 20 February 2019
1385-8947/

received much research attention in an attempt to overcome these drawbacks. Binary TMOs which have good electrical conductivity, a more feasible oxidation state than unary TMOs, and high chemical and thermal stabilities have been proposed as promising anode materials [20–25]. Moreover, better capacity and cycling stability of anodes can be achieved when two transition metals are incorporated into the host layer [26–28]. In particular, binary Ni-Co oxides have received research attention owing to their high redox activities and because the Ni and Co nanoparticles formed during the reduction process act as catalysts for the reversible conversion of Li_2O [29–33]. However, the pulverization of Ni-Co oxides because of a large volume variation during the charge–discharge process hinders their practical application to LIBs. Therefore, Ni-Co oxide nanostructures with various designs, such as hollow, yolk–shell, nanosheet, nanoplate, and nanotube structures, and carbon composites of these nanostructures have been proposed to buffer the volume change of electrode materials and effectively release the stress generated during cycling [34–41]. For example, Park et al. [34] synthesized three-dimensional macroporous carbon nanotube (CNT) microspheres highly loaded with $NiCo_2O_4$ hollow nanospheres by the spray pyrolysis process by making use of the nanoscale Kirkendall diffusion effect. The microspheres delivered a reversible discharge capacity of 572 mA h g^{-1} after 500 cycles at a current density of 3.0 A g^{-1}. Chen et al. [35] also prepared graphene-based $NiCo_2O_4$ nanosheet arrays directly grown on nickel foam by a hydrothermal reaction. Their discharge capacity was 806 mA h g^{-1} at a current density of 300 mA g^{-1}; this discharge capacity was maintained after 55 cycles. Rong et al. [36] synthesized a core–shell-structured $NiCo_2O_4$@GO hybrid composite (where GO denotes graphene oxide) by a hydrothermal reaction and post heat-treatment. The composite showed an initial discharge capacity of 1047 mA h g^{-1} at a current density of 50 mA g^{-1}, with a capacity retention of 77.6% after 100 cycles. However, more elaborate structural design and a facile synthetic strategy for anode materials are required in order to improve the Li-ion storage capacity of Ni-Co oxides for commercial use.

In the present study, we introduce a hierarchical yolk–shell-structured microsphere comprising a hierarchical CNT-(NiCo)O/C yolk and an embossed hollow thin shell [hereafter denoted as CNT-(NiCo)O/C] as a potential anode material for high-performance LIBs. This unique nanostructure was prepared by one-pot spray pyrolysis in a few seconds without any additional tedious process. During the spray pyrolysis process, the skeleton-like yolk, whose frame was linked with CNTs, was formed by mutual binding of the CNTs and size-controlled polystyrene (PS) nanobeads and subsequent selective decomposition of these nanobeads. The synergetic effects of the unique hierarchical yolk structure, protective hollow shell, and high-electrical-conductivity CNTs led to efficient lowering of Li-ion diffusion induced stresses during cycling, enhancement of the electrical conductivity, shortening of the Li-ion diffusion path, and improvement in the structural stability during cycling. As a consequence, extremely long cycle life stability, high reversible capacity, and superior rate properties of anodes could be achieved using the unique nanostructure proposed in this study. The CNT-(NiCo)O/C microspheres synthesized by a facile one-pot process are promising for practical use as anodes having superior Li-ion storage performance.

2. Experimental section

Sample preparation: The hierarchical yolk–shell-structured CNT-(NiCo)O/C microspheres were prepared by a one-pot spray pyrolysis process. Details of the spray pyrolysis system used for this purpose are shown in Fig. S1. In brief, droplets were generated using a 1.7 MHz ultrasonic spray generator that consisted of six vibrators, and the droplets were transported to a quartz tube reactor (length: 1200 mm, diameter: 50 mm) using N_2 carrier gas (flow rate: 10 L min^{-1}). The reactor temperature was fixed at 700 °C. The spray solution was prepared by dissolving 0.055 M nickel(II) nitrate hexahydrate [Ni $(NO_3)_2{\cdot}6H_2O$, Junsei, 98.0%], 0.11 M cobalt(II) nitrate hexahydrate [Co $(NO_3)_2{\cdot}6H_2O$, Samchun, 98.0%], and 4 g PVP (Mw: 40,000, Samchun) in 400 mL distilled water. Next, both 1.0 g CNTs and 10 g PS nanobeads (size: 100 nm) were added to the above solution, which was then stirred vigorously. In order to prepare the spray solution, CNTs (Cheap Tubes Inc., Cambridgeport, USA; OD: 20–30 nm, length: 10–30 μm, purity: > 95.0 wt%) were acid-treated via dispersion in HNO_3/H_2SO_4 (1:3 vol%) solution at 80 °C and washed with distilled water. Additionally, uniform-sized PS nanobeads (100 nm in size) were also prepared by an emulsifier-free emulsion polymerization method, which is described in detail in our previous work [42]. For comparison purposes, bare $(NiCo)O_x$ microspheres with a hollow structure were also prepared by one-pot spray pyrolysis under air atmosphere from a solution almost identical to that described above but without CNTs and PS nanobeads.

Characterization techniques: The microstructures of the samples were observed by field-emission scanning electron microscopy (Ultra Plus, Zeiss) and field-emission TEM (JEOL, JEM-2100F). Phase analysis was performed by XRD (Bruker D8 Discover with GADDS) using Cu Kα radiation (λ = 1.5418 Å). The structure of the carbonaceous materials in the microspheres was characterized via Raman spectroscopy (Jobin Yvon LabRam, HR800; excitation source: 514 nm He–Ne laser) at room temperature. An XPS instrument (Thermo Scientific, K-Alpha) with focused monochromatic Al Kα radiation at 12 kV and 20 mA was used to analyze the composition of the samples. The surface areas of the samples were measured by the BET method using N_2 as the adsorbate gas. TGA was performed using a thermogravimetric analyzer (Pyris 1 TGA, Perkin–Elmer) in the temperature range of 25–700 °C at a heating rate of 10 °C min^{-1} in air.

Electrochemical measurements: The electrochemical properties of the samples were measured by constructing 2032-type coin cells. The cell electrode was prepared by mixing 70 wt% active material, 20 wt% carbon black (Super-P) as a conductive material, and 10 wt% sodium carboxymethyl cellulose (CMC) as a binder. Lithium metal and a microporous polypropylene film were used as the counter electrode and separator, respectively. The electrolyte was prepared by dissolving 1 M $LiPF_6$ in a 1:1 (v/v) mixture of fluoroethylene carbonate and dimethyl carbonate (FEC/DMC). The coin cell was assembled in an argon atmosphere in a glove box. The discharge–charge characteristics of the samples were measured at various current densities in the voltage range of 0.001–3.0 V. Cyclic voltammetry measurements were performed at a scan rate of 0.1 mV s^{-1}. The dimensions of the anode were 1.4 cm × 1.4 cm, and the mass loading was approximately 1.0 mg cm^{-2}. The electrochemical impedance was measured by EIS over a frequency range of 100 kHz to 10 MHz with a signal amplitude of 10 mV. For the full-cell test, dense $LiMn_2O_4$ nanoparticles were used as the cathode. The mass loadings of the active material were 0.98 mg cm^{-2} for the anode and 6.86 mg cm^{-2} for the cathode. Before assembly of the full-cell, the anode half-cell was assembled and prelithiated for several cycles in the voltage range of 0.001–3.0 V. The electrolyte for the full-cell was 1 M $LiPF_6$ dissolved in a 1:1 (v/v) mixture of ethylene carbonate and diethyl carbonate (EC/DEC). The electrochemical properties of the 2032-type coin full-cells were examined at 200 mA g^{-1} in the voltage range of 2.5–4.0 V. The electrode capacity was calculated according to the weight of the anode materials.

3. Results and discussion

In this study, a hierarchical yolk–shell-structured CNT-(NiCo)O/C microsphere was prepared by a one-pot spray pyrolysis process without any further treatment. The detailed formation mechanism of the unique nanostructure is depicted in Scheme 1. First, droplets containing uniformly distributed Ni and Co salts, poly(vinylpyrrolidone) (PVP), size-controlled PS nanobeads, and CNTs were generated using an ultrasonic nebulizer, which constituted the spray pyrolysis process (Scheme 1-①). As the initial step of this process, the droplets were transported to a

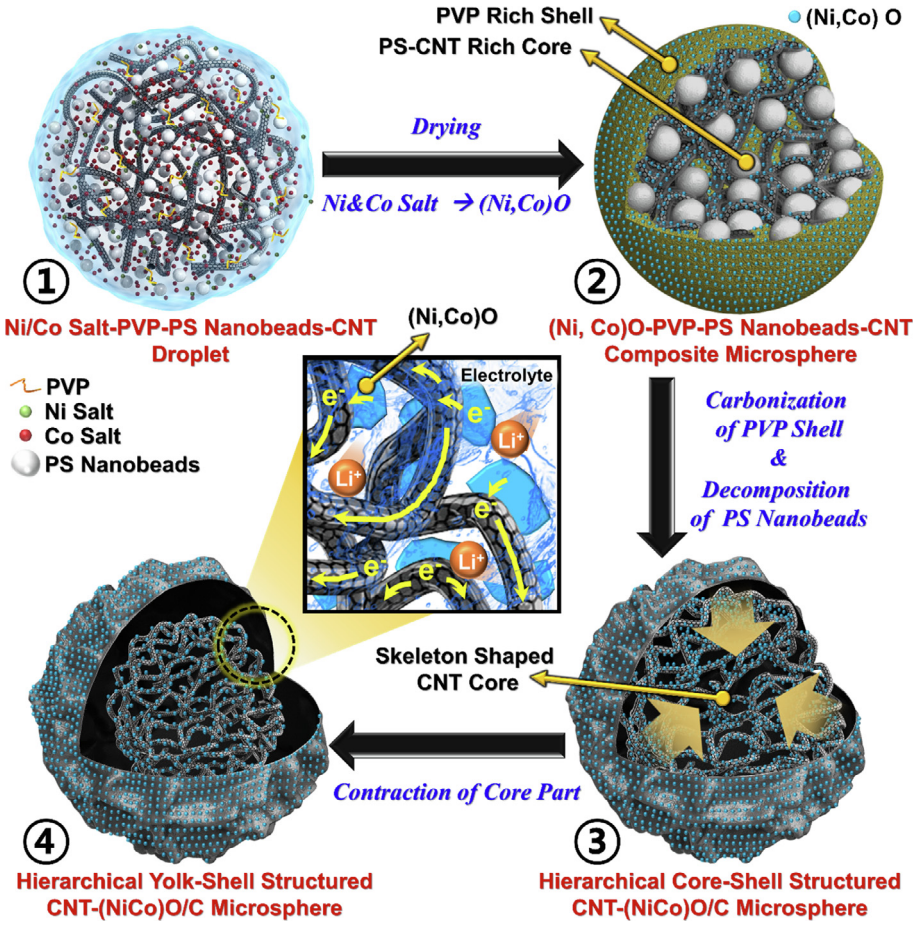

Scheme 1. Formation mechanism of the hierarchical yolk-shell structured CNT-(NiCo)O/C microsphere by one-pot spray pyrolysis.

high-temperature reactor using N_2 carrier gas and then dried. Subsequently, (Ni,Co)O solid-solution nanocrystals were uniformly formed in the structure by decomposition of the Ni and Co salts (Scheme 1-②). Notably, in this step, both a PVP-rich shell and a PS-CNT-rich core were formed in the microsphere of a dried droplet, as shown in Scheme 1-②. This formation can be explained as follows. PVP tended to migrate to the outside of the structure by phase separation from the metal salts, and concurrently, CNTs that coalesced with the PS nanobeads because of their high affinity migrated to the core part. In the next step, the PVP-rich shell was carbonized to form an amorphous carbon (AC) layer with (Ni,Co)O nanocrystals, as shown in Scheme 1-③. Simultaneously, the PS nanobeads gathered in the core part of the microsphere were selectively decomposed to a gaseous product, which resulted in the formation of numerous mesopores in the CNT-rich core part and a void layer inside the shell through contraction of the core part (Scheme 1-③). In the rear part of the tubular reactor, a void layer was formed through thermal contraction of the highly porous inner part of the composite during the spray pyrolysis process (Scheme 1-④). This consequently resulted in the formation of a skeleton-like porous yolk, whose frame was precisely linked with the CNTs. As a result, a hierarchical yolk–shell-structured CNT-(NiCo)O/C microsphere with a short residence time of 6 s inside the hot-wall reactor was obtained by the one-pot spray pyrolysis without any additional post-processing.

The individual functions of PVP, CNTs, and PS nanobeads in the spray solution and their mutual interactions during the synthesis of the hierarchical yolk–shell-structured microsphere were examined in detail. Fig. 1a,b shows the as-prepared powders obtained from the pure Ni-Co salt solution without PVP, CNTs, and PS nanobeads by spray pyrolysis. Most of the resulting powders showed broken shape of the microspheres. This is because PVP as a carbon source was not contained in the droplet, therefore Ni-Co salt materials could not aggregate as a microsphere during spray pyrolysis. Fig. 1a,b shows the as-prepared powders obtained from the Ni-Co salt solution with PVP and without the CNTs and PS nanobeads by spray pyrolysis. The resulting powders were hollow and spherical in shape and had a thin wall. This is because hollow microspheres are generally formed during spray pyrolysis owing to the fast drying of the droplets and the rapid decomposition of the Ni and Co salts. Similarly, the powders obtained from the Ni-Co salt solution containing PVP as well as added CNTs also showed a hollow morphology and had a thin wall, as shown in Fig. 1c,d. Although CNTs were added to the spray solution, they migrated to the outside of the shell along with PVP because of their affinity with PVP and formed the hollow shell. However, when the PS nanobeads were added to the PVP-containing Ni-Co salt solution, the morphology of the resulting powders changed distinctly from hollow to the hierarchical yolk–shell structure, as shown in Fig. 1e,f. In particular, the yolk showed a porous structure with interconnected mesopores. During the spray pyrolysis process, the melted PVP in the dried microsphere underwent phase separation and migrated outward, whereas the PS nanobeads gathered in the center and formed the PS-rich core. Subsequently, the PS nanobeads were decomposed, which resulted in the formation of the interconnected mesopores in the core. Subsequent formation of a void layer through thermal contraction of the highly porous inner part of the composite during the spray pyrolysis process resulted in the formation of the hierarchical yolk–shell structure.

In order to obtain an anode material with a high rate performance, CNTs with high electrical conductivity were additionally added to the Ni-Co salt solution containing PVP and the PS nanobeads. The morphologies of the resulting microspheres obtained from this solution by spray pyrolysis—denoted as CNT-(NiCo)O/C microspheres are

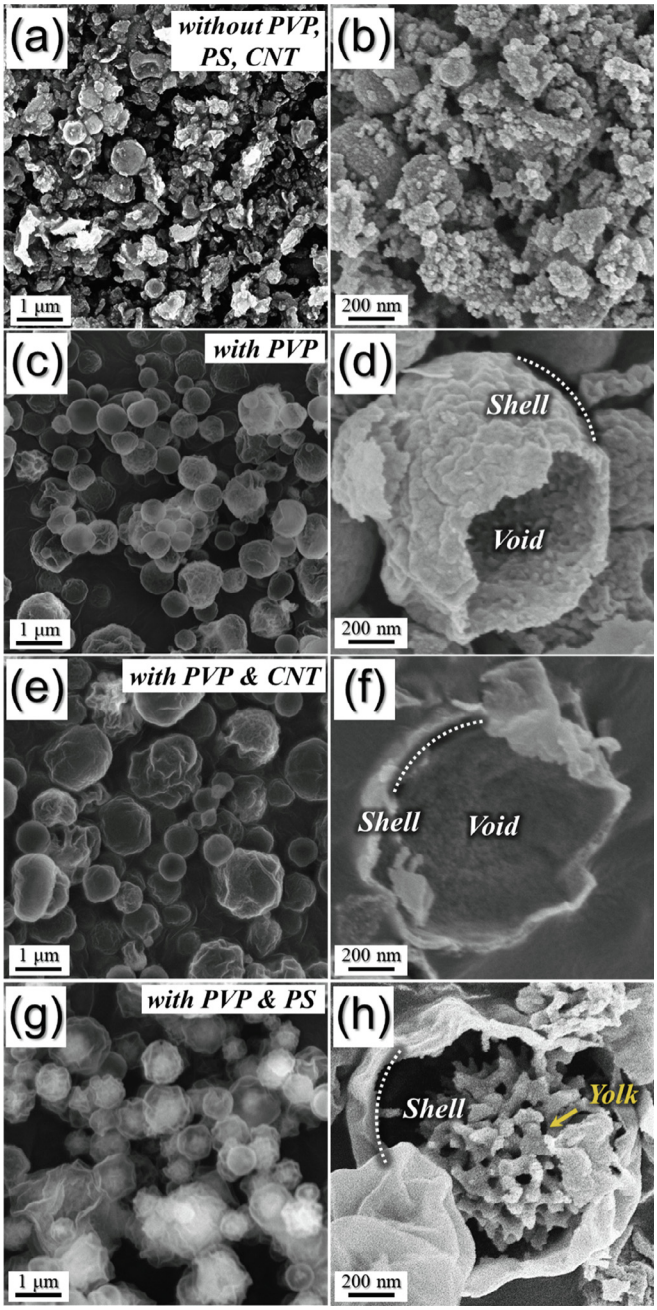

Fig. 1. SEM images of the as-prepared powders obtained after spray pyrolysis from the Ni/Co salt solution (a,b) without PVP, PS nanobeads, CNT, (c,d) with PVP, (e,f) with PVP and CNT, and (g,h) with PVP and PS nanobeads.

shown in Fig. 2. The overall powder morphology, shown in Fig. 2a, was spherical, and the powder had a wrinkled surface because of the thermal contraction of the shell into the internal space formed by the decomposition of the PS nanobeads during the spray pyrolysis process. The transmission electron microscopy (TEM) images of the microspheres in Fig. 2b,c reveal that they have a distinct yolk-void-shell configuration. Specifically, the yolk of the fractured microsphere shown in Fig. 2d has a skeleton-like sphere geometry similar to that of the powder obtained from the Ni-Co salt solution with PVP and PS and without CNTs (Fig. 1e,f). However, as shown in Fig. 2f, the frame of the skeleton-like yolk is composed of CNTs anchored to the (Ni,Co)O solid-solution nanocrystals, which is also confirmed from the X-ray diffraction (XRD) results (Fig. S2). This configuration is attributed to the fact that the CNTs, which had higher affinity to the PS nanobeads than to PVP, migrated to the core part along with the PS nanobeads during spray pyrolysis, after which the PS nanobeads were selectively decomposed. CNTs with a diameter of 20 nm were confirmed to constitute the frames, as indicated by the arrows in Fig. 2f. The high-resolution TEM image in Fig. 2g,h reveals that the shell part of the composite microsphere was composed of (Ni,Co)O nanocrystals 10–30 nm in size and surrounded by the AC layer. From Fig. 2h, the d-spacings corresponding to the (0 1 2) and (1 1 1) planes of the (Ni,Co)O solid solution were found to be 0.21 nm and 0.25 nm, respectively. The selected-area electron diffraction (SAED) pattern shown in Fig. 2i further confirmed the formation of the (Ni,Co)O nanocrystals during spray pyrolysis. Additionally, a diffraction ring corresponding to the (0 0 2) lattice confirmed the presence of the CNTs. The elemental mapping images shown in Fig. 2j revealed a homogeneous distribution of the (Ni,Co)O nanocrystals in the yolk–shell-structured carbon matrix.

The chemical state and molecular environment of the hierarchical yolk–shell-structured CNT-(NiCo)O/C microsphere were characterized by X-ray photoelectron spectroscopy (XPS) analysis, as shown in Fig. 3a–d. The XPS survey spectrum of the microsphere in Fig. 3a shows peaks corresponding to Ni, Co, O, and C signals. In the Co 2p XPS spectrum in Fig. 3b, peaks of Co $2p_{3/2}$ and Co $2p_{1/2}$ at 781.3 eV and 795.9 eV, respectively, and their corresponding satellite peaks were detected [34,43]. Additionally, peaks of Ni $2p_{3/2}$ and Ni $2p_{1/2}$ and their corresponding satellite peaks were detected at 853.94, 871.29, 859.2, and 882.1 eV, respectively, in the Ni 2p XPS spectrum (Fig. 3c) [34,43]. The XPS spectra of the CNT-(NiCo)O/C microsphere contained peaks of Co^{2+}, Ni^{2+}, and Ni^{3+} [34,43]. The atomic ratios of Co, Ni, and O elements in CNT-(NiCo)O/C microsphere were 13, 6, and 23%, respectively from the energy dispersive X-ray spectroscopy (EDS) results (Fig. S3). The additional peak corresponding to Ni^{3+} is attributed to the surface oxidation of the sample. The C 1s XPS spectrum in Fig. 3d includes peaks corresponding to C═O, C–O, C–C, and C═C bonds at 288.1, 286.2, 284.7, and 283.8 eV, respectively [34]. The higher intensity of the C–C peak than of the other peaks confirms the thermal reduction of the oxidized CNTs during spray pyrolysis. The Raman spectrum shown in Fig. 3e includes characteristic wide D- and G-bands of carbon at around 1340 cm^{-1} and 1590 cm^{-1}, respectively. The ratio of the peak intensity of the D-band to that of the G-band (I_D/I_G), which is commonly used to confirm structural disorders in graphitic materials, was found to be 0.78. The highly ordered CNTs in the CNT-(NiCo)O/C microsphere contributed to the high intensity of the G-band, although disordered AC was formed by the decomposition of PVP [24]. Thermogravimetric analysis (TGA) was performed in order to confirm the amounts of AC and CNTs in the nanostructure, as shown in Fig. 3f. The observed weight loss between 300 °C and 350 °C in the TG curve indicates that the nanostructure of the CNT-(NiCo)O/C microsphere contains 21 wt% of carbon under the assumption that (Ni,Co)O is converted into the NiO and Co_3O_4 phases (from the XRD result in Fig. S4). The Brunauer–Emmett–Teller (BET) surface area of the hierarchical yolk–shell-structured CNT-(NiCo)O/C microsphere was found to be 60 m^2 g^{-1}, as shown in Fig. S5; this high BET surface area is attributed to the unique hierarchical nanostructure of the CNT-(NiCo)O/C microsphere and the carbon contents of the CNTs and AC in the structure.

In order to verify the structural advantages of the hierarchical yolk–shell-structured CNT-(NiCo)O/C microsphere from the viewpoint of its Li-ion storage capacity, hollow microspheres without carbon [hereafter denoted as $(NiCo)O_x$] were also prepared as reference material by spray pyrolysis using the PVP-containing Ni-Co salt solution under air atmosphere. The hollow microspheres were found to be 500 nm in size, as shown in Fig. S6a,b. From the XRD results (Fig. S6c), the resulting microspheres were found to be composed of (Ni,Co)O and $NiCo_2O_4$ solid solutions. The oxygen-rich $NiCo_2O_4$ phase was formed under air atmosphere during spray pyrolysis. Additionally, the oxygen-deficient (Ni,Co)O phase was also formed by carbothermal reduction during the spray pyrolysis process. The negligible weight change in the

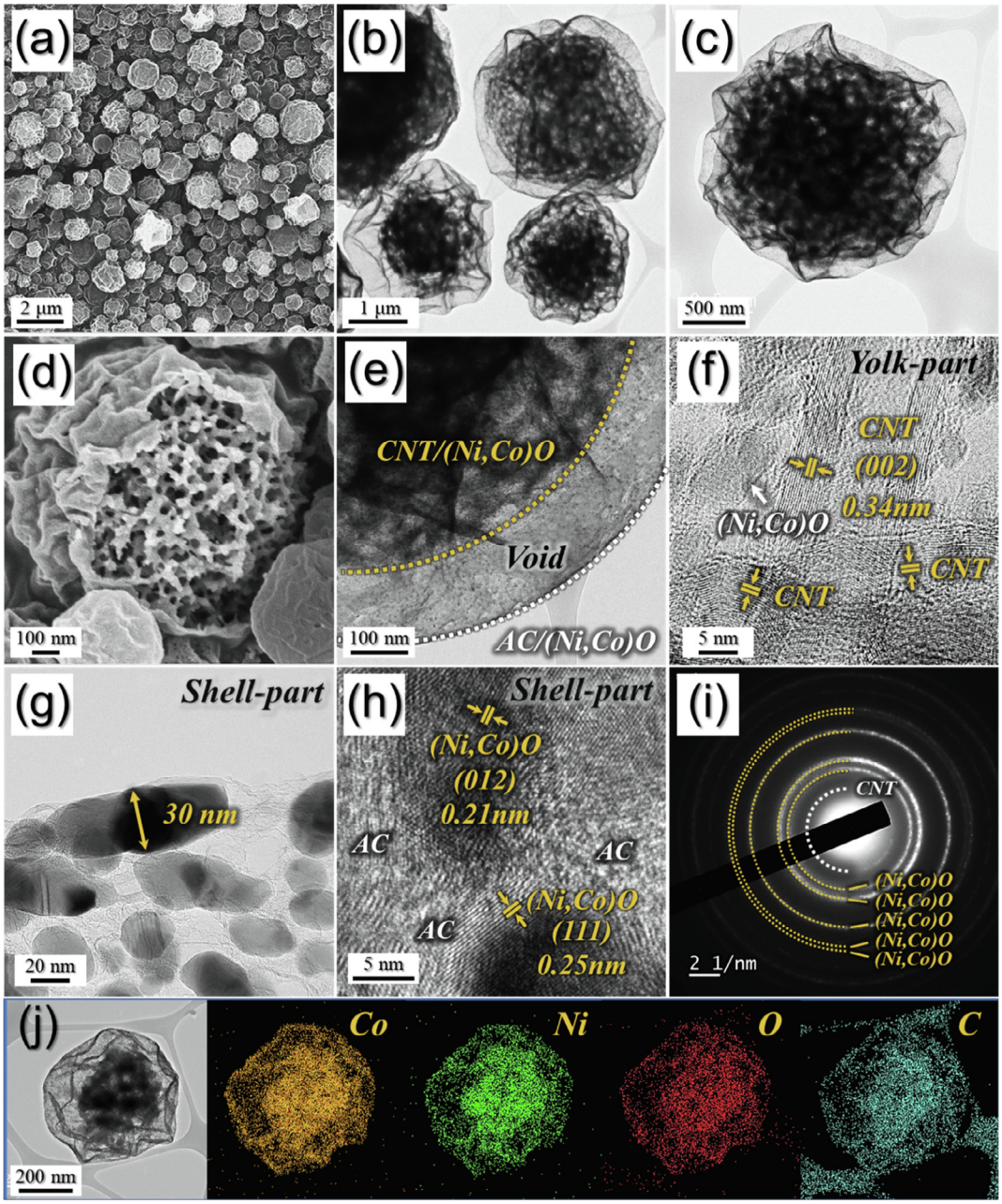

Fig. 2. Morphologies, SAED pattern, and elemental mapping images of CNT-(NiCo)O/C microspheres obtained after one-pot spray pyrolysis: (a,d) FE-SEM images, (b,c) TEM images, (e-h) HR-TEM images, (i) SAED pattern, and (j) elemental mapping images.

TG curve (Fig. S6d) confirmed the formation of $(NiCo)O_x$ microspheres without carbon.

The electrochemical properties of the hierarchical yolk–shell-structured CNT-(NiCo)O/C microspheres in comparison with those of the hollow $(NiCo)O_x$ microspheres are shown in Fig. 4. Cyclic voltammograms (CVs) of the CNT-(NiCo)O/C microspheres in the potential range of 0.001–3.0 V (*vs.* Li/Li^+) for the first 5 cycles at a scan rate of 0.1 mV s^{-1} are shown in Fig. 4a. The first cathodic scan of the CNT-(NiCo)O/C microspheres includes three cathodic peaks at 1.4, 0.4, and 0.2 V. The first peak at 1.4 V is attributed to the irreversible reaction between the surface functional groups of the CNTs and the Li-ions in the nanostructure [34,44,45]. The subsequent intense peak at 0.4 V is attributed to the reduction of the (Ni,Co)O nanoparticles into metallic Ni and Co crystals and to the formation of Li_2O and a solid electrolyte interface (SEI) layer [34,46]. The peak at 0.4 V shifted to a higher potential of 1.0 V from the 2nd cycle onward because of the conversion of the (Ni,Co)O nanocrystals into ultrafine nanocrystals during the 1st cycle [34,45,46]. Additionally, a peak related to the intercalation of the Li-ions into the CNTs and AC matrix appeared as a shoulder at around 0.2 V [44,45]. The peaks at 1.2 V and 2.3 V in the anodic scan of the CNT-(NiCo)O/C microspheres are attributed to the transformation of metallic Ni and Co into the NiO and CoO phases, respectively [34,45,46]. In contrast, the initial reduction peak at 0.9 V in the first cathodic CV curve of the hollow $(NiCo)O_x$ microspheres is attributed to the reduction of $NiCo_2O_4$ into metallic Ni and Co and the formation of amorphous Li_2O and the SEI layer [47,48]. The subsequent reduction peak at 0.5 V is attributed to the conversion of (Ni,Co)O into metallic Ni and Co nanocrystals [34,47,48]. Two broad peaks at 1.5 V and 2.2 V are observed in the anodic scan of the hollow $(NiCo)O_x$ microspheres, both of which are attributed to the oxidation of Ni and Co nanograins into NiO and CoO, respectively [34,48]. The first discharge–charge profiles of both the samples at a high current density of 5.0 A g^{-1} are shown in

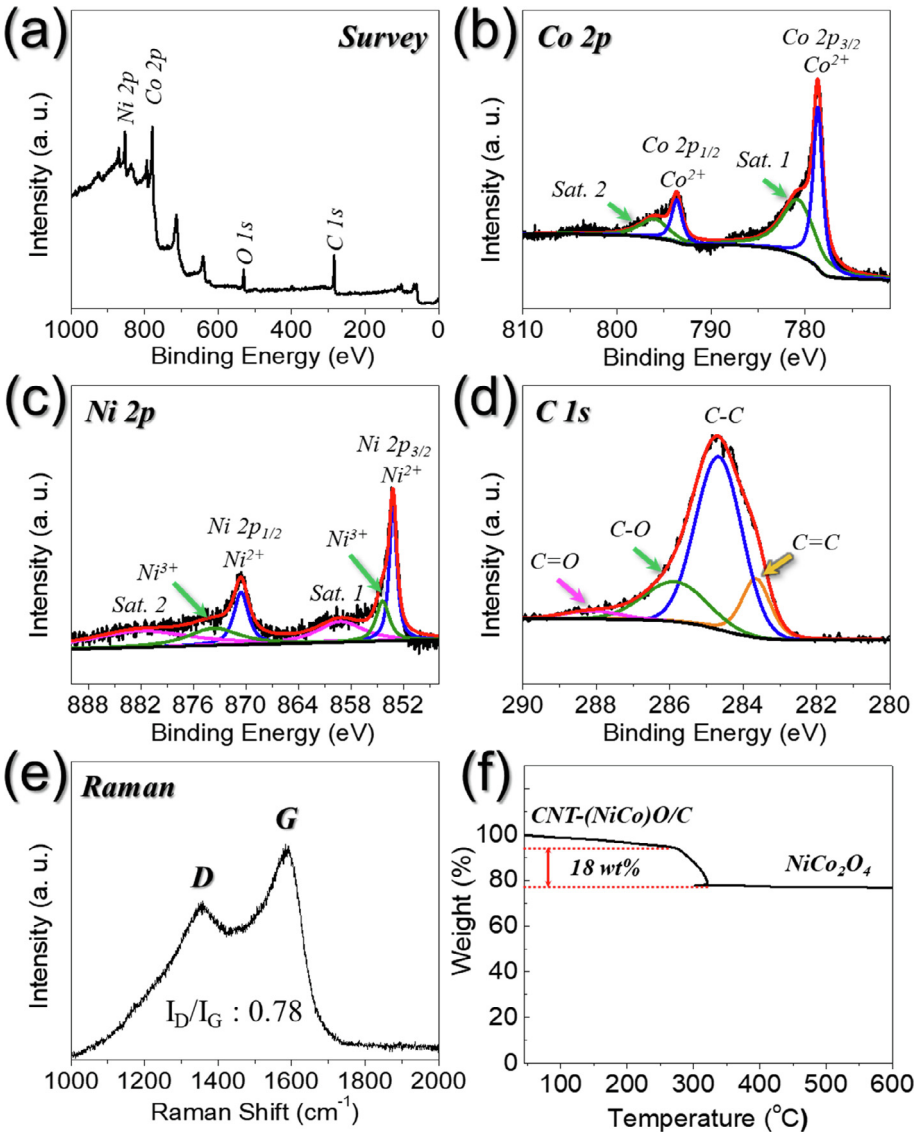

Fig. 3. (a) Survey XPS spectrum, (b) Co 2p XPS spectrum, (c) Ni 2p XPS spectrum, (d) C 1s XPS spectrum, (e) Raman spectrum, and (f) TGA curve of CNT-(NiCo)O/C microspheres.

Fig. 4b. The initial discharge capacities of the CNT-(NiCo)O/C and hollow (NiCo)O_x microspheres were 1016 mA h g^{-1} and 940 mA h g^{-1}, respectively, and their corresponding initial Coulombic efficiencies (CEs) were 64% and 65%, respectively. Although the CNT-(NiCo)O/C microspheres contained large amounts of carbonaceous materials, i.e., CNTs and AC, which have high initial irreversible capacity loss, both the samples had similar initial CEs. The low CE of the hollow (NiCo)O_x microspheres is attributed to the presence of $NiCo_2O_4$ in their structure. The irreversible phase conversion of $NiCo_2O_4$ in the 1st cycle led to a high initial capacity loss of the hollow (NiCo)O_x microspheres [49–51].

The long-term cycling performances of the two types of microspheres at a high current density of 5.0 A g^{-1} are shown in Fig. 4c. The discharge capacities of the hollow (NiCo)O_x microspheres decreased rapidly to 328 mA h g^{-1} after the 300th cycle because the carbon-free hollow structure could not accommodate the large strain induced by the volume variation of the active materials at a high current density. In contrast, the CNT-(NiCo)O/C microspheres showed superior long-term cycle properties even at an extremely high current density of 5.0 A g^{-1} for 1000 cycles. The discharge capacity of the CNT-(NiCo)O/C microspheres after 1000 cycles was 598 mA h g^{-1} and its corresponding CE was 99.1%. Moreover, the capacity retention of these microspheres after 1000 cycles as calculated from the 2nd cycle onward was 89%. The skeleton-like (NiCo)O/CNT yolk, the hollow space between the yolk and the shell, and the hollow carbon shell layer provided a degree of buffering against volume changes that accompany Li-ion insertion–desertion processes, thereby preventing pulverization and agglomeration of the electrode and consequently improving the structural stability during long-term cycling at an extremely high current density. The excellent rate performance of the CNT-(NiCo)O/C microspheres was compared with the rate performance of the hollow (NiCo)O_x microspheres, as shown in Fig. 4e. The CNT-(NiCo)O/C microspheres had high reversible discharge capacities of 886, 854, 802, 763, 709, 668, 620, 594, 560, 509, 462, 421, 352, and 294 mA h g^{-1} at current densities of 0.5, 1, 2, 3, 5, 7, 10, 12, 15, 20, 25, 30, 40, and 50 A g^{-1}, respectively. In addition, the discharge capacity recovered well to 991 mA h g^{-1} when the current density was reduced to 0.5 A g^{-1}, even after operation at extremely high current densities. The CNTs and AC present in the structure contributed to the high electrical conductivity of the CNT-(NiCo)O/C microspheres, which promoted the electron transfer kinetics; this consequently led to the improved Li-ion diffusion rate. Additionally, the porous (Ni,Co)O/AC shell and the skeleton-like CNT yolk with interconnected mesopores facilitated efficient

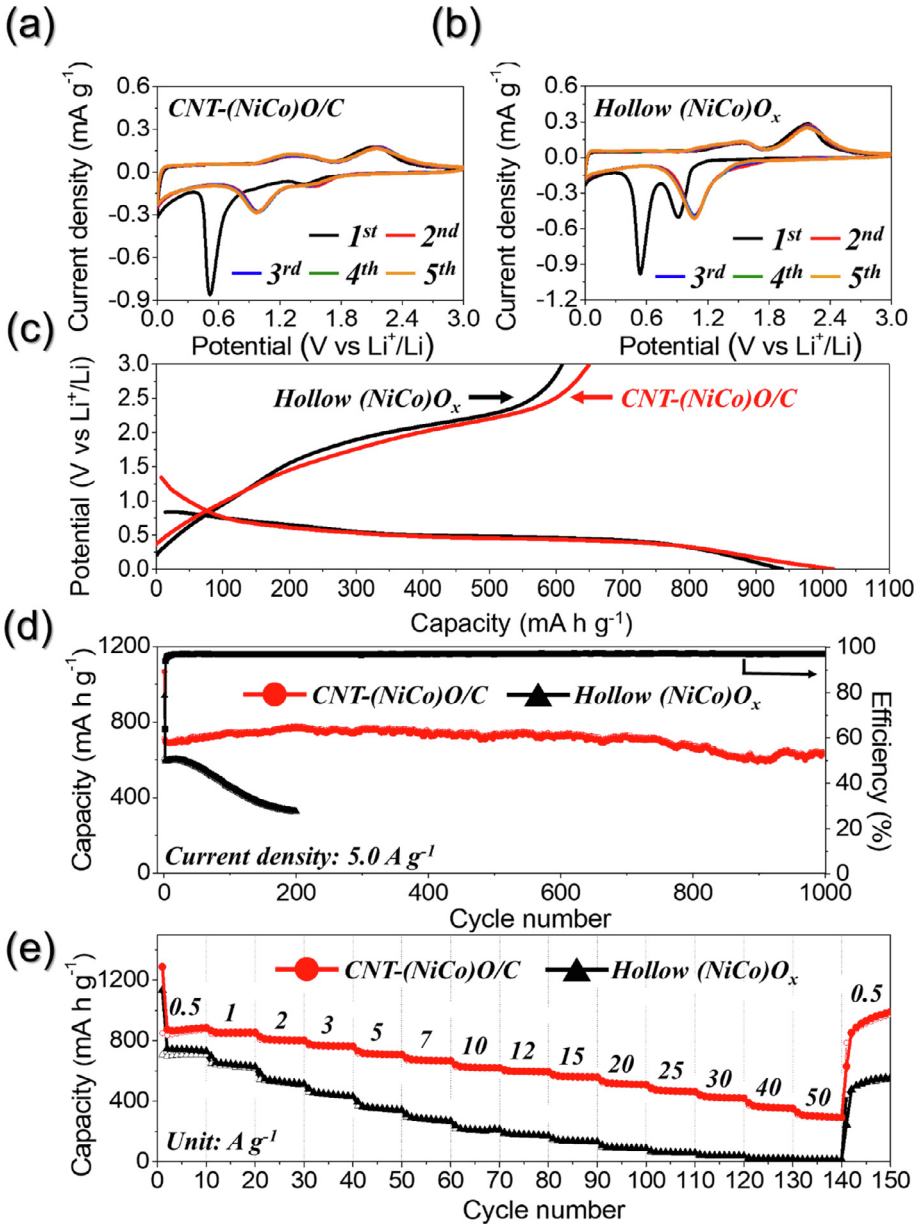

Fig. 4. Electrochemical properties of CNT-(NiCo)O/C and hollow (NiCo)O_x microspheres: (a) CV curves of CNT-(NiCo)O/C microspheres, (b) CV curves of hollow (NiCo)O_x microspheres, (c) initial discharge and charge profiles, (d) cycle properties at a current density of 5.0 A g^{-1}, and (e) rate properties.

infiltration of the electrolyte into the structure, which caused shortening of the diffusion pathways for the Li-ions and electrons. In contrast, the hollow (NiCo)O_x microspheres showed very low discharge capacities that decreased from 730 mA h g^{-1} to 13 mA h g^{-1} as the current density increased from 0.5 A g^{-1} to 50 A g^{-1}.

In order to examine the electrochemical properties of the CNT-(NiCo)O/C microspheres, they were subjected to electrochemical impedance spectroscopy (EIS) measurements before cycling and after the 1st, 100th, and 300th cycles in a fully charged state. The Nyquist plots shown in Fig. 5 consist of compressed semicircles in the medium-frequency range, which represent the charge-transfer resistance (R_{ct}) of the electrode, whereas the line inclined at ~45° to the real axis represents Li-ion diffusion into the electrodes [52–55]. Before cycling (see Fig. 5a), both types of microspheres had low and similar R_{ct} values of 38 Ω irrespective of their morphologies. After the 1st cycle, the R_{ct} values of both types of microspheres decreased owing to the formation of ultrafine nanocrystals during the 1st cycle (see Fig. 5b,c). However, the Nyquist plots showed a distinctly different pattern as the cycle number increased to 100 and 300. R_{ct} of the CNT-(NiCo)O/C microspheres remained almost constant at a low value of 17 Ω for 300 cycles because of its high structural stability. However, with an increase in the number of cycles, the R_{ct} value of the hollow (NiCo)O_x microspheres increased abruptly because of structural destruction during the cycles, as shown in Fig. 5c. The relationship between the real part of the impedance (Z_{re}) and $\omega^{-1/2}$ after 300 cycles (where ω is the angular frequency in the low-frequency region, given as $\omega = 2\pi f$) is shown in Fig. 5d. The less steep slope at low frequencies indicates higher Li-ion diffusivity in the CNT-(NiCo)O/C microspheres. The calculated lithium ion diffusion coefficients were 2.2×10^{-14} for CNT-(NiCo)O/C and 3.5×10^{-16} for the hollow (NiCo)O_x microsphere. Because of their higher electrical conductivity, the CNTs and AC promoted the electron transfer kinetics, which led to the improved Li-ion diffusion rate. Fig. 6 shows the morphologies of the CNT-(NiCo)O/C microspheres and hollow (NiCo)O_x microspheres obtained after 100 cycles at a current density 5.0 A g^{-1}. The morphology of the CNT-(NiCo)O/C microspheres was maintained quite well even after repeated lithiation–delithiation

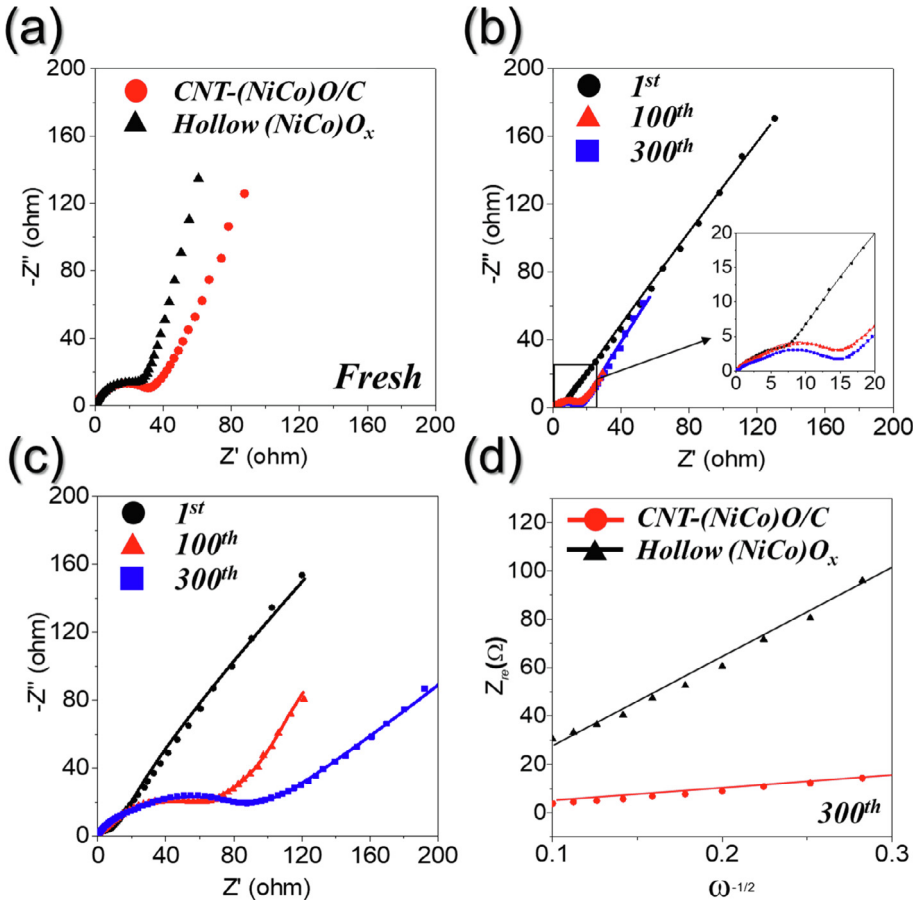

Fig. 5. (a-c) Nyquist impedance plots (lines represents fitting data) and (d) relationships between the real part of the impedance (Z_{re}) and $\omega^{-1/2}$ of CNT-(NiCo)O/C and hollow (NiCo)O_x microspheres: (a) before cycling, (b) after 1, 100, and 300 cycles of CNT-(NiCo)O/C, (c) after 1, 100, and 300 cycles of hollow (NiCo)O_x.

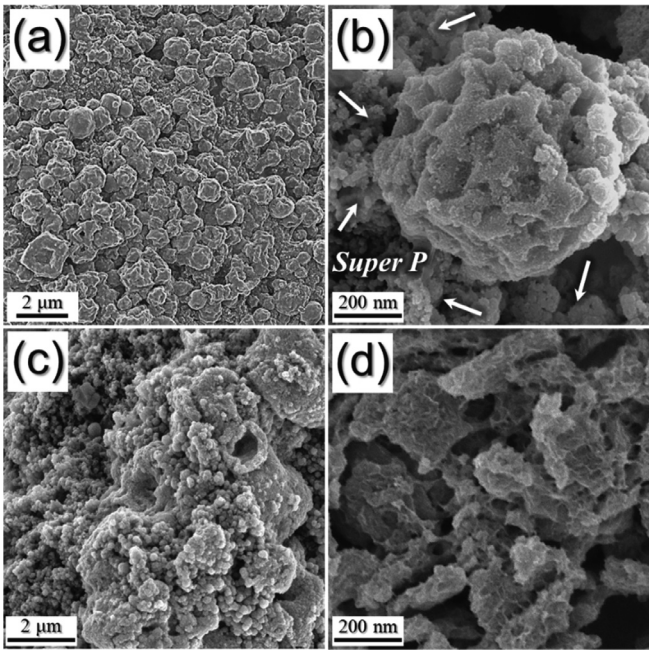

Fig. 6. SEM images of (a,b) CNT-(NiCo)O/C microspheres and (c,d) hollow (NiCo)O_x microspheres after 100 cycles.

processes because of their high structural stability, as shown in Fig. 6a,b. On the other hand, the hollow (NiCo)O_x microspheres failed to withstand the internal stress because of volume variation and fragmented into several pieces after 100 cycles, as shown in Fig. 6c.

In order to evaluate the commercial applicability of the unique nanostructure synthesized in this study, an anode composed of the CNT-(NiCo)O/C microsphere was prelithiated and combined with a $LiMn_2O_4$ cathode for a Li-ion full-cell test. The properties of the prepared $LiMn_2O_4$ nanoparticles used as the cathode are shown in Figs. S7 and S8. The charge and discharge curves of CNT-(NiCo)O/C@$LiMn_2O_4$ full-cells with a cut-off voltage in the range of 2.5–4.0 V are shown in Fig. 7. In the 1st cycle, the full-cell showed charge and discharge capacities of 130.2 mA h g^{-1} and 113.3 mA h g^{-1}, respectively, at a current density of 200 mA g^{-1}, based on the $LiMn_2O_4$ cathode mass. The initial CE of the full-cell was 87%, and it increased rapidly to 99% in the subsequent cycles. The charge and discharge capacities of the full-cell after 500 cycles were 88.3 mA h g^{-1} and 88.1 mA h g^{-1}, respectively. The CNT-(NiCo)O/C@$LiMn_2O_4$ full-cell exhibited excellent cyclic performance during the lithiation–delithiation process. Fig. 7c shows a digital photographic image of light-emitting diode (5 V, 10 mW) powered by the two-cell battery in tandem and its voltage output.

4. Conclusions

A hierarchical yolk–shell-structured microsphere comprising a hierarchical CNT-(NiCo)O/C yolk and an embossed hollow thin shell, with a short residence time of 6 s in a hot-wall reactor, was prepared by a one-pot spray pyrolysis process. During the spray pyrolysis process, the hierarchical CNT-(NiCo)O/C yolk, whose frame was linked with the CNTs, was formed by mutual binding of the CNTs and size-controlled polystyrene (PS) nanobeads and subsequent selective decomposition of these nanobeads. The skeleton-like (Ni,Co)O/CNT yolk, the hollow space between the yolk and the shell, and the hollow carbon shell layer

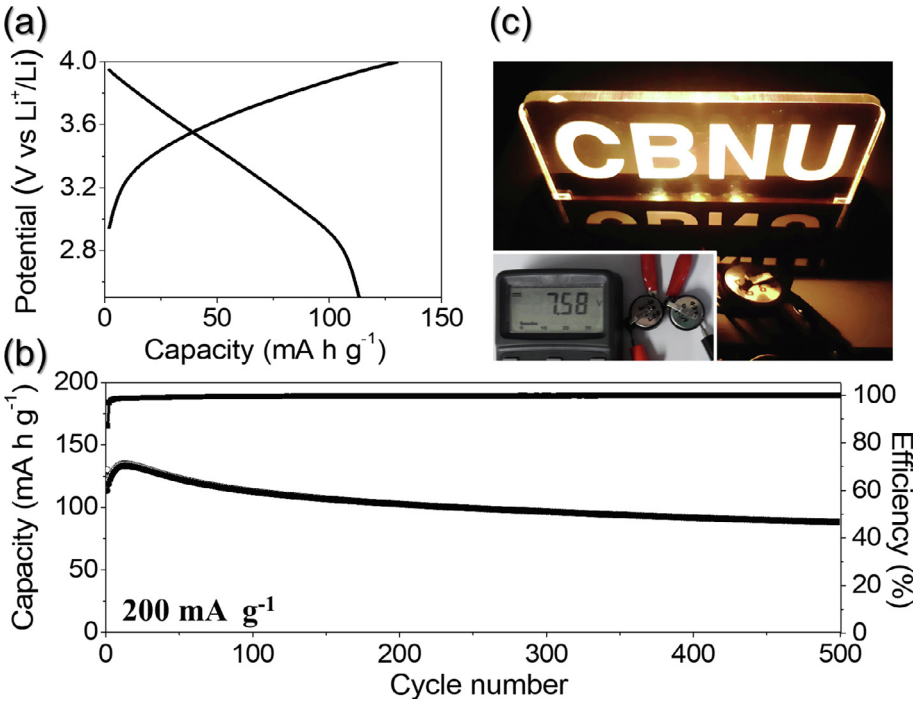

Fig. 7. Electrochemical properties of CNT-(NiCo)O/C@$LiMn_2O_4$ full-cell: a) initial charge/discharge curves, b) cycling performance at a current density of 200 mA g^{-1}, and c) digital photographic image of a light-emitting diode (5 V, 10 mW) powered by a two full cell battery in tandem and its voltage output.

provided a degree of buffering against volume changes during cycling, which improved the structural stability of the prepared microspheres during long-term cycling. Additionally, the CNTs and AC present in the structure contributed to the high electrical conductivity of the microspheres, which promoted the electron transfer kinetics; this consequently led to an improved Li-ion diffusion rate. Therefore, the CNT-(NiCo)O/C microspheres exhibited superior electrochemical properties in terms of Li-ion storage on account of their improved structural stability and electrical conductivity during repeated Li-ion insertion–desertion processes. The CNT-(NiCo)O/C microspheres synthesized by a facile one-pot process are promising for practical use as anodes having superior Li-ion storage performance.

Acknowledgment

This work was supported by the National Research Foundation of Korea (NRF) grant funded by the Korea government (MSIP) (NRF-2018R1A4A1024691, NRF-2017M1A2A2087577, and NRF-2018R1D1A3B07042514)

Appendix A. Supplementary data

Supplementary data to this article can be found online at https://doi.org/10.1016/j.cej.2019.02.144.

References

[1] M.-S. Balogun, Z. Wu, Y. Luo, W. Qiu, X. Fan, B. Long, M. Huang, P. Liu, Y. Tong, High power density nitridated hematite (α-Fe_2O_3) nanorods as anode for high-performance flexible lithium ion batteries, J. Power Sources 308 (2016) 7–17.
[2] J.S. Cho, Y.J. Hong, Y.C. Kang, Design and synthesis of bubble-nanorod-structured Fe_2O_3–carbon nanofibers as advanced anode material for Li-ion batteries, ACS Nano 9 (2015) 4026–4035.
[3] X. Han, W.-M. Chen, X. Han, Y.-Z. Tan, D. Sun, Nitrogen-rich MOF derived porous Co_3O_4/N–C composites with superior performance in lithium-ion batteries, J. Mater. Chem. A 4 (2016) 13040–13045.
[4] S.H. Oh, J.-S. Park, M.S. Jo, Y.C. Kang, J.S. Cho, Design and synthesis of tube-in-tube structured NiO nanobelts with superior electrochemical properties for lithium-ion storage, Chem. Eng. J. 347 (2018) 889–899.
[5] Y. Yang, B. Qiao, X. Yang, L. Fang, C. Pan, W. Song, H. Hou, X. Ji, Lithium titanate tailored by cathodically induced graphene for an ultrafast lithium ion battery, Adv. Funct. Mater. 24 (2014) 4349–4356.
[6] J. Wang, Q. Zhang, X. Li, D. Xu, Z. Wang, H. Guo, K. Zhang, Three-dimensional hierarchical Co_3O_4/CuO nanowire heterostructure arrays on nickel foam for high-performance lithium ion batteries, Nano Energy 6 (2014) 19–26.
[7] J. Chen, L. Xu, W. Li, X. Gou, α-Fe_2O_3 nanotubes in gas sensor and lithium-ion battery applications, Adv. Mater. 17 (2005) 582–586.
[8] J.S. Cho, S.Y. Lee, H.S. Ju, Y.C. Kang, Synthesis of NiO nanofibers composed of hollow nanospheres with controlled sizes by the nanoscale Kirkendall diffusion process and their electrochemical properties, ACS Appl. Mater. Interfaces 7 (2015) 25641–25647.
[9] Y. Chu, L. Guo, B. Xi, Z. Feng, F. Wu, Y. Lin, J. Liu, D. Sun, J. Feng, Y. Qian, S. Xiong, Embedding MnO@Mn_3O_4 nanoparticles in an N-doped-carbon framework derived from Mn-organic clusters for efficient lithium storage, Adv. Mater. 30 (2018) 1704244.
[10] X.W. Lou, D. Deng, J.Y. Lee, J. Feng, L.A. Archer, Self-supported formation of needlelike Co_3O_4 nanotubes and their application as lithium-ion battery electrodes, Adv. Mater. 20 (2008) 258–262.
[11] M.-S. Park, G.-X. Wang, Y.-M. Kang, D. Wexler, S.-X. Dou, H.-K. Liu, Preparation and electrochemical properties of SnO_2 nanowires for application in lithium-ion batteries, Angew. Chem. Int. Ed. 46 (2007) 750–753.
[12] Y.J. Yoo, Y.J. Hong, Y.C. Kang, Rationally designed microspheres consisting of yolk–shell structured $FeSe_2$–Fe_2O_3 nanospheres covered with graphitic carbon for lithium-ion batteries, J. Mater. Chem. A 6 (2018) 15182–15190.
[13] T. Li, Z. Wang, H. Guo, Y. Li, J. Wang, A new design concept for preparing nickel-foam-supported metal oxide microspheres with superior electrochemical properties, J. Mater. Chem. 5 (2017) 13469–13474.
[14] J.S. Cho, Y.C. Kang, Nanofibers comprising yolk–shell Sn@void@SnO/SnO_2 and hollow SnO/SnO_2 and SnO_2 nanospheres via the Kirkendall diffusion effect and their electrochemical properties, Small 11 (2015) 4673–4681.
[15] J.S. Cho, J.M. Won, J.-H. Lee, Y.C. Kang, Synthesis and electrochemical properties of spherical and hollow-structured NiO aggregates created by combining the Kirkendall effect and Ostwald ripening, Nanoscale 7 (2015) 19620–19626.
[16] X. Lu, D. Zheng, T. Zhai, Z. Liu, Y. Huang, S. Xie, Y. Tong, Facile synthesis of large-area manganese oxide nanorod arrays as a high-performance electrochemical supercapacitor, Energy Environ. Sci. 4 (2011) 2915–2921.
[17] S.A. Needham, G.X. Wang, H.K. Liu, Synthesis of NiO nanotubes for use as negative electrodes in lithium ion batteries, J. Power Sources 159 (2006) 254–257.
[18] F. Wang, H.-Y. Zhuo, X. Han, W.-M. Chen, D. Sun, Foam-like CoO@N, S-codoped carbon composites derived from a well-designed N, S-rich Co-MOF for lithium-ion batteries, J. Mater. Chem. A 5 (2017) 22964–22969.
[19] T. Li, Z. Wang, H. Guo, A short process for the efficient utilization of transition-metal chlorides in lithium-ion batteries: a case of $Ni_{0.8}Co_{0.1}Mn_{0.1}O_{1.1}$ and $LiNi_{0.8}Co_{0.1}Mn_{0.1}O_2$, J. Power Sources 342 (2017) 495–503.
[20] X.Q. Chen, H.B. Lin, X.W. Zheng, X. Cai, P. Xia, Y.M. Zhu, X.P. Li, W.S. Li, Fabrication of core–shell porous nanocubic Mn_2O_3@TiO_2 as a high-performance anode for lithium ion batteries, J. Mater. Chem. A 3 (2015) 18198–18206.
[21] Y. Qiu, S. Yang, H. Deng, L. Jin, W. Li, A novel nanostructured spinel $ZnCo_2O_4$

electrode material: morphology conserved transformation from a hexagonal shaped nanodisk precursor and application in lithium ion batteries, J. Mater. Chem. 20 (2010) 4439–4444.
[22] C. Yuan, H.B. Wu, Y. Xie, X.W. Lou, Mixed transition-metal oxides: design, synthesis, and energy-related applications, Angew. Chem. Int. Ed. 53 (2014) 1488–1504.
[23] G. Zhang, X.W. Lou, General synthesis of multi-shelled mixed metal oxide hollow spheres with superior lithium storage properties, Angew. Chem. 126 (2014) 9187–9190.
[24] Y. Zhang, L. Li, H. Su, W. Huang, X. Dong, Binary metal oxide: advanced energy storage materials in supercapacitors, J. Mater. Chem. A 3 (2015) 43–59.
[25] J. Leng, Z. Wang, X. Li, H. Guo, H. Li, K. Shih, C. Yan, J. Wang, Accurate construction of a hierarchical nickel–cobalt oxide multishell yolk–shell structure with large and ultrafast lithium storage capability, J. Mater. Chem. A 5 (2017) 14996–15001.
[26] Y.J. Hong, J.S. Cho, Y.C. Kang, Superior electrochemical properties of nanofibers composed of hollow $CoFe_2O_4$ nanospheres covered with onion-like graphitic carbon, Chem. Eur. J. 21 (2015) 18202–18208.
[27] S.H. Choi, S.K. Park, J.-K. Lee, Y.C. Kang, Facile synthesis of multi-shell structured binary metal oxide powders with a Ni/Co mole ratio of 1:2 for Li-Ion batteries, J. Power Sources 284 (2015) 481–488.
[28] X. Zhong, X. Wang, H. Wang, Z. Yang, Y. Jiang, J. Li, Z. Tian, Ultrahigh-performance mesoporous $ZnMn_2O_4$microspheres as anode materials for lithium-ion batteries and their *in situ* Raman investigation, Nano Res. 11 (2018) 3814–3823.
[29] J. Li, S. Xiong, Y. Liu, Z. Ju, Y. Qian, High electrochemical performance of monodisperse $NiCo_2O_4$ mesoporous microspheres as an anode material for Li-ion batteries, ACS Appl. Mater. Interfaces 5 (2013) 981–988.
[30] X. Xu, B. Dong, S. Ding, C. Xiao, D. Yu, Hierarchical $NiCoO_2$ nanosheets supported on amorphous carbon nanotubes for high-capacity lithium-ion batteries with a long cycle life, J. Mater. Chem. A 2 (2014) 13069–13074.
[31] J. Zhu, Z. Xu, B. Lu, Ultrafine Au nanoparticles decorated $NiCo_2O_4$ nanotubes as anode material for high-performance supercapacitor and lithium-ion battery applications, Nano Energy 7 (2014) 114–123.
[32] C.H. Kim, J.-W. Jung, K.R. Yoon, D.-Y. Youn, S.J. Park, I.-D. Kim, A high-capacity and long-cycle-life lithium-ion battery anode architecture: silver nanoparticle-decorated SnO_2/NiO nanotubes, ACS Nano 10 (2016) 11317–11326.
[33] Y. Qi, H. Zhang, N. Du, C. Zhai, D. Yang, Synthesis of Co_3O_4@SnO_2@C core-shell nanorods with superior reversible lithium-ion storage, RSC Adv. 2 (2012) 9511–9516.
[34] G.D. Park, J.-K. Lee, Y.C. Kang, Three-dimensional macroporous CNTs microspheres highly loaded with $NiCo_2O_4$ hollow nanospheres showing excellent lithium-ion storage performances, Carbon 128 (2018) 191–200.
[35] Y. Chen, J. Zhu, B. Qu, B. Lu, Z. Xu, Graphene improving lithium-ion battery performance by construction of $NiCo_2O_4$/graphene hybrid nanosheet arrays, Nano Energy 3 (2014) 88–94.
[36] H. Rong, Y. Qin, Z. Jiang, Z.-J. Jiang, M. Liu, A novel $NiCo_2O_4$@GO hybrid composite with core-shell structure as high-performance anodes for lithium-ion batteries, J. Alloy. Compd. 731 (2018) 1095–1102.
[37] Y. Chen, M. Zhuo, J. Deng, Z. Xu, Q. Li, T. Wang, Reduced graphene oxide networks as an effective buffer matrix to improve the electrode performance of porous $NiCo_2O_4$nanoplates for lithium-ion batteries, J. Mater. Chem. A 2 (2014) 4449–4456.
[38] H. Hou, M. Jing, Y. Yang, Y. Zhu, L. Fang, W. Song, C. Pan, X. Yang, X. Ji, Sodium/lithium storage behavior of antimony hollow nanospheres for rechargeable batteries, ACS Appl. Mater. Interfaces 6 (2014) 16189–16196.
[39] T. Li, X. Li, Z. Wang, H. Guo, Y. Li, A novel $NiCo_2O_4$ anode morphology for lithium-ion batteries, J. Mater. Chem. A 3 (2015) 11970–11975.
[40] Y. Mo, Q. Ru, X. Song, S. Hu, L. Guo, X. Chen, 3-dimensional porous $NiCo_2O_4$ nanocomposite as a high-rate capacity anode for lithium-ion batteries, Electrochim. Acta 176 (2015) 575–585.
[41] N. Zhang, Y. Wang, M. Jia, Y. Liu, J. Xu, L. Jiao, F. Cheng, Ultrasmall Sn nanoparticles embedded in spherical hollow carbon for enhanced lithium storage properties, Chem. Commun. 54 (2018) 1205–1208.
[42] S.Y. Jeong, S.-K. Park, Y.C. Kang, J.S. Cho, One-dimensional nanostructure comprising $MoSe_2$ nanosheets and carbon with uniformly defined nanovoids as an anode for high-performance sodium-ion batteries, Chem. Eng. J. 351 (2018) 559–568.
[43] X. Wang, W. Li, X. Wang, J. Zhang, L. Sun, C. Gao, J. Shang, Y. Hu, Q. Zhu, Electrochemical properties of $NiCoO_2$ synthesized by hydrothermal method, RSC Adv. 7 (2017) 50753–50759.
[44] G. Gao, Y. Jin, Q. Zeng, D. Wang, C. Shen, Carbon nanotube-wrapped Fe_2O_3 anode with improved performance for lithium-ion batteries, Beilstein J. Nanotechnol. 8 (2017) 649.
[45] S. Klink, E. Ventosa, W. Xia, F.L. Mantia, M. Muhler, W. Schuhmann, Tailoring of CNT surface oxygen groups by gas-phase oxidation and its implications for lithium ion batteries, Electrochem. Commun. 15 (2012) 10–13.
[46] A.K. Mondal, D. Su, S. Chen, K. Kretschmer, X. Xie, H.J. Ahn, G. Wang, A microwave synthesis of mesoporous $NiCo_2O_4$ nanosheets as electrode materials for lithium-ion batteries and supercapacitors, ChemPhysChem 16 (2015) 169–175.
[47] X. Wang, L. Qiao, X. Sun, X. Li, D. Hu, Q. Zhang, D. He, Mesoporous NiO nanosheet networks as high performance anodes for Li ion batteries, J. Mater. Chem. A 1 (2013) 4173–4176.
[48] J.-S. Park, J.S. Cho, J.H. Kim, Y.J. Choi, Y.C. Kang, Electrochemical properties of micron-sized Co_3O_4 hollow powders consisting of size controlled hollow nanospheres, J. Alloy. Compd. 689 (2016) 554–563.
[49] R. Hu, H. Zhang, Y. Bu, H. Zhang, B. Zhao, C. Yang, Porous Co_3O_4 nanofibers surface-modified by reduced graphene oxide as a durable, high-rate anode for lithium ion battery, Electrochem. Acta 228 (2017) 241–250.
[50] L. Luo, J. Wu, J. Xu, V.P. Dravid, Atomic resolution study of reversible conversion reaction in metal oxide electrodes for lithium-ion battery, ACS Nano 8 (2014) 11560–11566.
[51] Q. Su, J. Zhang, Y. Wu, G. Du, Revealing the electrochemical conversion mechanism of porous Co_3O_4 nanoplates in lithium ion battery by *in situ* transmission electron microscopy, Nano Energy 9 (2014) 264–272.
[52] J. Chen, W. Song, H. Hou, Y. Zhang, M. Jing, X. Jia, X. Ji, Ti^{3+} self-doped dark rutile TiO_2 ultrafine nanorods with durable high-rate capability for lithium-ion batteries, Adv. Funct. Mater. 25 (2015) 6793–6801.
[53] F. Cheng, J. Chen, Transition metal vanadium oxides and vanadate materials for lithium batteries, J. Mater. Chem. 21 (2011) 9841–9848.
[54] C. Liang, T. Zhai, W. Wang, J. Chen, W. Zhao, X. Lu, Y. Tong, Fe_3O_4/reduced graphene oxide with enhanced electrochemical performance towards lithium storage, J. Mater. Chem. A 2 (2014) 7214–7220.
[55] J.-S. Park, S.Y. Jeong, K.M. Jeon, Y.C. Kang, J.S. Cho, Iron diselenide combined with hollow graphitic carbon nanospheres as a high-performance anode material for sodium-ion batteries, Chem. Eng. J. 339 (2018) 97–107.